Transport of Non-Newtonian Suspensions of Highly Concentrated Micro- And Nanoscale Iron Particles in Porous Media: A Modeling Approach

Original
Transport of Non-Newtonian Suspensions of Highly Concentrated Micro- And Nanoscale Iron Particles in Porous Media: A Modeling Approach / Tosco, T.A.E., Sethi, R.. - In: ENVIRONMENTAL SCIENCE & TECHNOLOGY. - ISSN 0013-936X. - 44:23(2010), pp. 9062-9068. [10.1021/es100868n]

Publisher:
American Chemical Society

Published
DOI:10.1021/es100868n

Author's version
Published in
Environmental Science & Technology 44(23), pp 9062-9068
DOI: 10.1021/es100868n
http://dx.doi.org/10.1021/es100868n

Transport of non-Newtonian suspensions of highly concentrated micro- and nanoscale iron particles in porous media: a modeling approach

Tiziana Tosco, Rajandrea Sethi

DITAG – Dipartimento di Ingegneria del Territorio, dell'Ambiente e delle Geotecnologie,

Politecnico di Torino, Corso Duca degli Abruzzi, 24, 10129 Torino (Italy)

October 8th, 2010

Corresponding author: Dr. Rajandrea Sethi, rajandrea.sethi@polito.it. Phone: +390115647735. Fax: +390115647699

ABSTRACT: The use of zerovalent iron micro- and nanoparticles (MZVI and NZVI) for groundwater remediation is hindered by colloidal instability, causing aggregation (for NZVI) and sedimentation (for MZVI) of the particles. Transportability of MZVI and NZVI in porous media was previously shown to be significantly increased if viscous shear-thinning fluids (xanthan gum solutions) are used as carrier fluids. In this work, a novel modeling approach is proposed and applied for the simulation of 1D flow and transport of highly concentrated (20 g/l) non-Newtonian suspensions of MZVI and NZVI, amended with xanthan gum (3 g/l). The coupled model is able to simulate the flow of a shear thinning fluid accounting for the variable apparent viscosity arising from changes in xanthan and suspended iron particle concentrations. The transport of iron particles is modeled using a dual-site approach accounting for straining and physico-chemical deposition/release phenomena. A general formulation for reversible deposition is herein proposed, that includes all commonly applied dynamics (linear attachment, blocking, ripening). Clogging of the porous medium due to deposition of iron particles is modeled by tying porosity and permeability to deposited iron particles. The numerical model proved to adequately fit the transport tests conducted using both MZVI and NZVI and can develop into a powerful tool for the design and the implementation of full scale zerovalent iron applications.

Introduction

Engineered micro- and nano-materials are characterized by promising properties that can be exploited for the treatment of contaminated matrixes *(1-2)*. Injectable Fe-based particles have been extensively studied in recent years for the remediation of a broad range of contaminants in aquifer systems, or to enhance microbial activity *(3-5)*. Nano-sized (NZVI) as well as micro-sized (MZVI) zerovalent iron particles are an improvement as compared to commonly used granular iron *(6-7)*: suspended in a slurry, these colloidal dispersions can be directly injected to target the source of contamination, overcoming most of the limitations of zerovalent iron-based permeable reactive barriers (PRBs) *(2)*. Although the technology is still under development, successful field scale applications make it extremely promising *(8)*.

Beside reactivity, one of the key issues towards the implementation of NZVI and MZVI is assessing their transport mechanisms during injection into the subsurface (i.e. at high particles concentrations, pressures and flow velocities), and later under natural flow conditions. Particle mobility is highly desired during injection and in the early stages of migration, to guarantee an acceptable spacing between injection points and to ensure a uniform distribution of the iron slurry in the contaminated area. However, previous studies have shown that the transport of unmodified NZVI and MZVI suspensions is strongly limited by their colloidal instability *(9-12)*. Although NZVI primary particles are in the order of tens of nanometers, much larger dendritic aggregates are formed due to the strong magnetic attractive interactions *(13)*, which then undergo straining in porous media (i.e. are retained in small and dead-end pores *(14)*). Magnetic interactions also lead to ripening phenomena during subsurface filtration, which result in a progressive clogging of the porous matrix *(15)*. MZVI mobility, in turn, is considerably affected by sedimentation, due to the large size of the microparticles. Consequently, its mobility is strongly limited, and would be insufficient for any field application *(12)*.

To prevent particle aggregation and settling, two main strategies can be adopted. Usually, a surface modification via adsorption of polymers is used for NZVI *(16-18)*: polymeric chains form a soft “shell” around the particles *(17-18)*, providing electrostatic, steric, or electrosteric stabilization. As an alternative, highly concentrated NZVI (but also the less stable MZVI) can be stabilized by modification of the rheological properties of the dispersant fluid. Previous studies have shown that biodegradable polymers, namely xanthan gum, are effective in providing both steric and viscous (kinetic) stabilization of iron slurries *(12, 19)*. Xanthan was found to be a good carrier for highly concentrated NZVI and MZVI suspensions *(12)*, increasing their column breakthrough, and facilitating the injection processes due to the shear thinning behavior of the dispersions *(20)*. Shear-thinning fluids are characterized by decreasing viscosity with increasing shear rate. Consequently, xanthan solutions can enhance stability of the iron dispersion when the product is stored (as high viscosity prevents gravitational settling and aggregation of the particles), and do not hinder the injection operations, that are conducted at high shear rates (thus reducing the viscosity of the fluid).

Modeling iron transport during injection and under natural conditions is of pivotal importance for the interpretation of lab tests and in order to design and implement effective field applications. A wide literature is available on modeling colloid transport in groundwater systems, particularly referred to naturally occurring particles, such as microorganisms (for the risk they represent for human health) and clays or oxides (that are known to act as carriers for strongly sorbing contaminants). Models are commonly based on a modified advection-dispersion equation, including exchange terms describing particle deposition onto the soil matrix, and the consequent release. Concentration-dependent deposition rates for the simulation of blocking and ripening phenomena are commonly used *(21-22)* and spatial-dependent sites have been adopted to mimic mechanical filtration or straining *(23)*. Conversely, mechanistic approach provides a physical justification of the macroscopic deposition/release coefficients *(24-25)*. In both approaches, the Newtonian fluid flow and colloidal transport equations are solved independently, or are only weakly or empirically coupled *(23, 26-27)*. However, when dealing with iron suspensions, ripening and straining can often lead to a progressive clogging of the porous medium. Therefore, hydrodynamic parameters and fluid properties cannot be considered independent on the concentration of deposited and suspended particles *(28)*. Clogging phenomena are usually simulated using a filter-averaged approach, mostly for wastewater treatment applications *(28)*. Other studies are related to the change in pore space geometry due to mineral precipitation *(29)* or microbial growth *(30-31)*.

In this study, colloid transport is modeled using a dual-site (physico-chemical interactions and straining) advection-dispersion-deposition equation. A general formulation for attachment/detachment dynamics is herein proposed, capable to describe all commonly used deposition mechanisms and kinetics, namely linear attachment, blocking, ripening. The influence of colloid transport on porosity, permeability, and fluid viscosity is explicitly included into the model. The shear-thinning behavior of the iron slurries is described including a variable apparent viscosity in Darcy’s law *(32)*. The set of model equations is implemented in a finite-differences code, that represents the extension of the MNM1D model, previously proposed by the authors for the simulation of colloid transport under transient ionic strength *(27)*. The model is used to fit 1D column tests conducted at highly concentrated (20 g/l) slurries of MZVI and NZVI dispersed in a non-Newtonian gel of xanthan gum (3 g/l) *(12)*.

Theory and mathematical modeling

In the following paragraphs the non-Newtonian flow and colloidal transport model is presented. Clogging effects are modeled by defining state equations for viscosity of the mobile phase and for porosity, both expressing the dependence of these parameters on the amount of deposited or suspended particles. A modified Cross model *(33)* is formulated, describing the viscosity of shear-thinning suspensions of NZVI and MZVI particles as a function of shear rate, particle and xanthan concentration. Clogging of porous medium is modeled through changes of permeability, used here as a proxy, which is function of the deposited particles. Clogging and non-Newtonian properties of the pore fluid are included in variable (time and space dependent) permeability and viscosity coefficients. Therefore, a modified Darcy’s law for non-Newtonian fluids is adopted. As for the transport of particles, a novel formulation for particle attachment/detachment dynamics is proposed.

The proposed formulation relies on the hypotheses of 1D horizontal quasi-stationary flow, constant discharge, and negligible compressibility of particles, porous matrix, pore fluid, and particles deposits.

Porosity. The void space of the porous medium (characterized by the clean bed porosity n) can be filled by (i) the immobile deposited particles, characterized by a volume fraction ε_s, and (ii) the mobile phase, with a volume fraction $\varepsilon_m = n - \varepsilon_s$, which comprises the pore fluid (water, viscous solution of xanthan, etc.) and the suspended particles. During the transport of highly concentrated suspensions of iron particles, the effects of attachment, detachment, and straining processes determine a change of the volume fraction ε_m available for the flow, from the initial clean bed porosity, n, with a progressive clogging of the medium, due to the accumulation of particles in the solid phase:

$$\varepsilon_m(s) = n - \varepsilon_s = n - \frac{\rho_b}{\rho_s} s \qquad (1)$$

where ε_m is the volume fraction of the mobile phase, ρ_b is the porous medium bulk density [ML^{-3}], s is mass of retained particles per unit mass of porous medium [-], and ρ_s is the density of particle deposits [ML^{-3}].

Permeability. Modification of porosity and specific surface area of the porous matrix, due to the deposition of particles, affects the permeability of the porous medium. According to Kozeny *(34)*, the permeability depends on the third power of porosity and on the inverse square of the specific surface area of the matrix, which evolves from the clean bed surface area a_0 [L^{-1}] according to the following expression:

$$a(s) = a_0 + \theta a_p \frac{\rho_b}{\rho_p} s \qquad (2)$$

where θ is the fraction of the surface area of the deposited particles a_p [L^{-1}] that contributes to the increase of the surface area of the matrix, and ρ_p is the density of the particles [M L^{-3}]. The higher is θ (always lower than 1), the more irregular and dendritic is the particle deposit.

The derived expression for the permeability K [L ^{2}] is therefore:

$$K(s) = K_0 \left[\frac{\varepsilon_m(s)}{n} \right]^3 \left(\frac{a_0}{a_0 + \vartheta a_p \dfrac{\rho_b}{\rho_p} s} \right)^2 \tag{3}$$

where K_0 is the clean bed permeability (corresponding to porosity n and specific surface area a_0).

Mobile phase viscosity. The dependence of the dynamic viscosity of xanthan-stabilized suspensions of iron particles on shear rate $\dot{\gamma}$ [T^{-1}] can be expressed by an extended Cross model *(33)* accounting for both xanthan and particle concentration:

$$\mu_m(\dot{\gamma}_m, c, c_x) = \mu_{m,\infty} + \frac{\mu_{m,0}(c, c_x) - \mu_{m,\infty}}{1 + \left[\lambda_m(c) \times \dot{\gamma} \right]^{\chi_m(c)}} \tag{4}$$

where c is the concentration of suspended particles [ML^{-3}], c_x is the xanthan concentration, $\lambda_m(c)$ is the so-called Cross time constant [T], $\chi_m(c)$ is the Cross rate constant [-], $\mu_{m,0}(c, c_x)$ is the zero shear viscosity, and $\mu_{m,\infty}$ is the asymptotic viscosity at high shear rates, here assumed to be equal to pure water viscosity.

Previous studies *(35-36)* have shown that zero shear viscosity is significantly affected by both xanthan and iron particles concentrations. Because of the relatively small xanthan concentration (0-3 g/l), a linear dependence on this parameter can be introduced according to the following expression:

$$\mu_{m,0}(c, c_x) = \mu_{m,\infty} + \frac{\left[\mu^*_{m,0}(c) - \mu_{m,\infty} \right]}{c_x^*} c_x = \mu_{m,\infty} + M(c)\, c_x \tag{5}$$

where $\mu^*_{m,0}$ is the zero shear viscosity measured at the xanthan concentration c^*_x, and the dependence on iron nanoparticles concentration is lumped inside the function $M(c)$ that can be derived from experimental data. Relationships for the other Cross parameters as functions of particle and xanthan concentration are reported elsewhere *(35)* and a brief description is provided in the Supporting Information.

The “shear rate in porous medium”, i.e. the apparent shear rate experienced by a fluid flowing through a porous medium *(37-38)* is:

$$\dot{\gamma}_m = \alpha_\gamma \frac{q_m}{\sqrt{K\varepsilon_m}} \tag{6}$$

where q_m is the darcyan velocity [LT^{-1}], and the shift factor α_γ is introduced to superimpose rheograms obtained from rotational tests and flow through porous medium *(39)*.

Darcy’s law. Under laminar conditions, non-Newtonian effects can be lumped into the porous medium viscosity coefficient (μ_m), while the deposition of particles over time modifies the hydraulic conductivity. The pressure gradient is therefore related to the specific discharge of the fluid phase (constant during the tests) according to:

$$\frac{\partial p}{\partial x} = -\frac{\mu_m}{K} q_m \tag{7}$$

where p is the pressure, and K and μ_m are defined by eq. (3), (4), and (5) .

Colloid transport equations. The iron particle transport is governed by a coupled set of equations describing the advection and dispersion phenomena in the liquid phase and the multisite interaction processes with the solid phase:

$$\begin{cases} \dfrac{\partial}{\partial t}(\varepsilon_m c) + \sum\limits_i \left(\rho_b \dfrac{\partial s_i}{\partial t} \right) = -\dfrac{\partial}{\partial x}(q_m c) + \dfrac{\partial}{\partial x}\left(\varepsilon_m D \dfrac{\partial c}{\partial x} \right) \\ \rho_b \dfrac{\partial s_i}{\partial t} = f_i(c, s_i) \end{cases} \tag{8}$$

where D is the hydrodynamic dispersion [L^{2}T^{-1}].

The second equation represents the generic interaction site with the solid phase, which can model physico-chemical attachment/detachment processes with linear, blocking or ripening dynamics, straining etc.

A general formulation of reversible attachment/detachment dynamics is here proposed (Figure 1), which can be adapted both to blocking or ripening phenomena:

$$\rho_b \frac{\partial s_i}{\partial t} = \varepsilon_m k_{a,i}\left(1 + A_i s^{\beta_i}\right)c - \rho_b k_{d,i} s_i \qquad (9)$$

where $k_{a,i}$ is the deposition rate [T^{-1}], $k_{d,i}$ is the release rate (eventually equal to zero for irreversible deposition) [T^{-1}], and A_i [-] and β_i [-] are respectively the multiplier and exponent coefficients that define the interaction dynamics.

For $A_i > 0$ and $\beta_i > 0$, the deposition rate increases with increasing concentration of attached particles, thus resulting in a ripening dynamics. Conversely, for $\beta_i = 1$, $A_i = -1/s_{\max,i}$ the blocking model is obtained, being $s_{\max,i}$ the maximum concentration of particles that can be deposited for the i-th interaction site. For $A_i = 0$ the linear reversible model is found.

Non-Newtonian flow and transport model. The complete set of equations is therefore:

$$
\begin{aligned}
&\frac{\partial p}{\partial x} = -\frac{\mu_m}{K} q_m \\
&\frac{\partial}{\partial t}\left(\varepsilon_m c\right) + \frac{\partial\left(\rho_b s_1\right)}{\partial t} + \frac{\partial\left(\rho_b s_2\right)}{\partial t} = -\frac{\partial}{\partial x}\left(q_m c\right) + \frac{\partial}{\partial x}\left(\varepsilon_m D \frac{\partial c}{\partial x}\right) \\
&\frac{\partial\left(\rho_b s_1\right)}{\partial t} = \varepsilon_m k_{a,1}\left(1 + A_1 s^{\beta_1}\right) c - \rho_b k_{d,1} s_1 \\
&\frac{\partial\left(\rho_b s_2\right)}{\partial t} = \varepsilon_m k_{a,2}\left(1 + \frac{x}{d_{50}}\right)^{\beta_2} c - \rho_b k_{d,2} s_2 \\
&\frac{\partial}{\partial t}\left(\varepsilon_m c_x\right) = -\frac{\partial}{\partial x}\left(q_m c_x\right) + \frac{\partial}{\partial x}\left(\varepsilon_m D \frac{\partial c_x}{\partial x}\right) \\
&\mu_m\left(\dot{\gamma}_m, c, c_x\right) = \mu_{m,\infty} + \frac{M(c) c_x}{1 + \left[\lambda_m(c) \cdot \dot{\gamma}_m\right]^{\chi_m(c)}} \\
&K(s) = K_0\left[\frac{\varepsilon_m}{n}\right]^3 \left(\frac{a_0}{a_0 + \vartheta a_p \dfrac{\rho_b}{\rho_p} s}\right)^2 \\
&\dot{\gamma}_m(s) = \alpha_\gamma \frac{q_m}{\sqrt{K \varepsilon_m}} \\
&\varepsilon_m(s) = n - \frac{\rho_b}{\rho_s} s
\end{aligned}
\qquad (10)
$$

where d_{50} is the mean diameter of the porous material [L] and c_x is the xanthan concentration which is simulated as a conservative species.

Two interaction sites are considered: S1, for deposition and release due to physico-chemical phenomena following the general kinetics (9), and S2, for a reversible straining site using Bradford’s approach *(23, 40)*.

Attachment coefficients for both interaction sites were calculated according to the following expression, in order to account for transients in xanthan concentrations:

$$
k_{a,i}\left(c_x\right) = k_{ax,i} \frac{c_x}{c_{x,0}} + k_{aw,i}\left(1 - \frac{c_x}{c_{x,0}}\right) \qquad (11)
$$

where $c_{x,0}$ is the injected xanthan concentration and $k_{a,i} = k_{ax,i}$ during injection ($c_x = c_{x,0}$), $k_{a,i} = k_{aw,i}$ during flushing ($c_x = 0$). Detachment coefficients are calculated in a similar way.

Materials and methods

Detailed description of materials and methods for the column tests here simulated was provided in a previous work *(12)*. See Supporting Information for further details.

Materials. Commercial powders of MZVI (BASF-HQ, Germany) and suspensions of NZVI (RNIP-10DS from Toda Kogyo Corp., Japan) were used for column transport experiments with silica sand (Sibelco, Italy). Iron particles at a concentration of 20 g/l were dispersed in xanthan solution (3 g/l, Jungbunzlauer, Switzerland) in DI water, or in xanthan solution in water with modified ionic strength (12.5 mM *(41)*).

Experimental protocol. Iron suspensions were injected in horizontal sand-packed saturated columns, 0.46 m long. The test protocol included a pre-conditioning with water (DI or 12.5 mM), an injection of 7 (or 26) PVs (pore volumes) of iron suspensions, a final flushing with 26 (or 15) PVs of DI (or 12.5mM) water.

Tests were named according to the injection protocol: N7X is NZVI injected for 7 PVs dispersed in xanthan with DI water, M26X is MZVI dispersed in xanthan and injected for 26 PVs; N7XIS is NZVI injected for 7 PV dispersed in xanthan with modified ionic strength, etc.

Inlet and outlet iron concentrations were measured in-line using two magnetic susceptibility sensors *(12)*. Also, the total iron concentration (in pore fluid and deposited on sand grains) was measured after slurry injection (before flushing) every 2 cm along the column using a non invasive coaxial susceptibility sensor. The pressure drop at the column ends was continuously monitored.

Numerical implementation and inversion of the model equations. The model equations (10) are implemented in a finite-difference scheme, thereby extending to iron slurries the approach adopted in previous works on colloid transport *(27, 42)*. The system of equations is solved iteratively using a Picard's scheme to derive the spatial and temporal evolution of the variables. Pressure drop is calculated integrating the pressure gradient over the entire length of the column L:

$$\Delta p\left(t;s,c,c_x\right) = -q_m\int_0^L \frac{\mu_m}{K}\,dx \tag{12}$$

For each test, the set of fitting parameters (Table 1) was determined by constrained non linear least squares fitting of experimental data using a large-scale algorithm based on the interior-reflective Newton method *(43)* and data regularization. Fitted parameters are ρ_s, θ, α_γ and the adhesion/release coefficients (4 coefficient for each fluid phase, plus 3 parameters common to both phases). Coefficients were determined via simultaneous fitting of breakthrough curves, pressure drop over time, and measured spatial distribution of total iron (Figure 3).

Results and discussion

Experimental and model fitted breakthrough curves, and pressure drop over time are reported in Figure 2 for all experiments. The model proved to accurately reproduce the experimental data under different conditions. Further confirmation of the reliability of the model and of the inversion procedure is provided by the comparison between results coming from short duration injection tests (M7X and N7X) and long injection tests (M26X and N26X).

Pressure drop curves. The pressure drop evolution over time (Figure 2d-f and j-l) is satisfactorily reproduced by the model, that includes the constitutive equation for change in viscosity, and it is also able to capture the progressive clogging of the porous medium. This phenomenon is shown by a linear increase of pressure drop during injection (especially in presence of nanoscale iron). The introduction of the apparent viscosity into the Darcy's law allows for a correct simulation of the stepwise pressure increase during injection, when xanthan solution displaces water. Nevertheless, it is worth to notice that the modeled curves usually exhibit a more abrupt descent at the beginning of the flushing, if compared to the more smoothed profile of the experimental measurements. This is probably due to the simple model adopted to simulate the transport of xanthan gum in fast transient conditions (i.e. at the early beginning of flushing).

Deposition and release dynamics. Simulated attachment/detachment coefficients (Table 1) and the corresponding simulated breakthrough curves (Figure 2) highlight, as a general rule, that attachment is lower during injection, higher during flushing. The difference among attachment coefficients for particles dispersed in water ($k_{aw,i}$) and xanthan ($k_{ax,i}$) is approximately one order of magnitude. This is in agreement with experimental evidence of increased stability of the suspensions provided by xanthan *(12)*. Straining was included in the model based on the observation of experimental profiles of retained particles (Figure 3), which show the typical shape of strained deposits *(14)*. Xanthan gum, characterized by an high molecular weight, is able to adsorb on the particles generating a brush layer that provides steric stabilization of the suspensions, but significantly increasing the overall hydrodynamic radius of the particle. No specific measurements are available in the literature for the thickness of the brush layer formed by xanthan molecules. However, the overall dimension of coated particles is likely to be in the order of few microns and therefore straining phenomena can occur.

Microiron (M26X, M7X and M7XIS, Figure 2a-c) tends to reach the influent concentration at the column outlet during the injection phase, thus suggesting that blocking phenomena are likely to occur (negative values of A_1). Both the concentration profiles of retained particles (Figure 3a) and mass balances (Supporting Information) confirm the occurrence of blocking: the percentage of eluted particles during injection is lower for short-lasting experiments (M7X and M7XIS), higher for the long-lasting experiment (M26X), showing that iron particles are retained mostly in the early stages of the test. Conversely, breakthrough curves for nanoiron (N26X, N7X, N7XIS, Figure 2g-i) tend to stabilize at concentrations slightly lower than the inlet, suggesting that particle deposition follows a ripening dynamics mechanism (9), modeled by positive values of A_1. Ripening has a negative impact on the medium permeability, thus producing the slow linear increase in pressure drop curves during injection (Figure 2j-l).

For tests M7XIS and N7XIS, breakthrough curves exhibit a more complex deposition/release dynamics if compared to results obtained for tests undertaken in DI water (Figure 2c, and i). MZVI follows a blocking dynamics mechanism ($A_1 < 0$), NZVI a ripening one ($A_1 > 0$), as well as for tests in DI water, and as expected. However, in these cases straining plays a relevant role, as suggested by the fitted coefficients (Table 1) and the concentration profiles (Figure S3 in Supporting Information). Particle release during flushing takes place in two steps: first, a rapid release of a small amount of iron is observed, followed by a slower release of larger quantities of microparticles. Lower amounts of particles are deposited in the physico-chemical interaction site during injection (see Supporting Infortmation and Figure 3a), and are then rapidly released at the early stages of flushing. Conversely, larger amounts are retained on the straining site, and slowly released during flushing, thus producing the abovementioned tailing effect. This behavior is evident in N7XIS. It is likely that changes in ionic strength do not only affect the electrical interactions among particles, but have also an effect on the brush layer. This process results in a more delayed release (and the consequent tailing in the breakthrough curves) in N7XIS if compared to M7XIS, where the inter-particles attraction is less pronounced due to absence of magnetic interactions *(12)*.

Concentration and permeability profiles.

As a general rule, the permeability decrease at the end of the injection (Figure 3b) is more pronounced for NZVI, less pronounced for MZVI tests. The permeability reduction is modeled here as the result of two contributions, namely the reduction of ε_m, and the increase of specific surface area, a. For all tests the latter was found to dominate (see Supporting Information for plots of these contributions), which is also in agreement with the literature *(28)*. Nevertheless, also reduction of ε_m was found not to be negligible, in particular for NZVI experiments, where the volume of deposited particles becomes quite relevant, due to ripening phenomena. This finding confirms that the use of equation (3) is appropriate when modeling clogging of the porous medium due to deposition of iron particles, including effects of changes in both porosity and specific surface area.

Environmental implications. The work herein presented, although implemented in one dimensional geometry for the interpretation of laboratory experiments, can be the first step of a modeling framework for field-scale design of MZVI- and NZVI- based interventions. The numerical model, here implemented for 1D- domains, can be extended to radial, spherical or general 3D geometries accounting for the change in velocities and shear rate over space and thus showing a more pronounced dependence on non-Newtonian behavior of the suspensions.

The concentration of iron particles and xanthan gum here considered are similar to those of full-scale applications. Field injections of iron-based slurries are usually performed with direct push equipments, which ensure an almost constant discharge in different lithologies and in time. The shear-thinning properties of xanthan gum provide colloidal stability of MZVI and NZVI slurries without hindering the injection, thanks to the low viscosity at high shear rates. Both experimental and modeling results show that MZVI stabilized using xanthan can be injected more easily, without significant retention in coarse sand, if compared to NZVI. However, the final choice of the particle size for field applications should derive from a careful balance between mobility and reactivity, which is likely to be on the side of NZVI.

References

1. Tratnyek, P.G.; Johnson, R.L. Nanotechnologies for environmental cleanup. *Nano Today* **2006**, *1*(2), 44-48.
2. Zhang, W.X. Nanoscale iron particles for environmental remediation: An overview. *J Nanopart Res* **2003**, *5*(3-4), 323-332.
3. Bosch, J.; Heister, K.; Hofmann, T.; Meckenstock, R.U. Nanosized iron oxide colloids strongly enhance microbial iron reduction. *Appl Environ Microbiol* **2010**, *76*(1), 184-9.
4. Liu, Y.Q.; Majetich, S.A.; Tilton, R.D.; Sholl, D.S.; Lowry, G.V. TCE dechlorination rates, pathways, and efficiency of nanoscale iron particles with different properties. *Environmental Science & Technology* **2005**, *39*(5), 1338-1345.
5. Xu, Z.; Dong, J. Synthesis, Characterization, and Application of Magnetic Nanocomposites for the Removal of Heavy Metals from Industrial Effluents. in *Emerging Environmental Technologies*; V. Shah, Editor; Springer, 2008.
6. Dries, J.; Bastiaens, L.; Springael, D.; Agathos, S.N.; Diels, L. Competition for sorption and degradation of chlorinated ethenes in batch zero-valent iron systems. *Environmental Science and Technology* **2004**, *38*(10), 2879-2884.
7. Di Molfetta, A.; Sethi, R. Clamshell excavation of a permeable reactive barrier. *Environmental Geology* **2006**.
8. He, F.; Zhao, D.Y.; Paul, C. Field assessment of carboxymethyl cellulose stabilized iron nanoparticles for in situ destruction of chlorinated solvents in source zones. *Water Research* **2010**, *44*(7), 2360-2370.
9. Cwiertny, D.M.; Handler, R.M.; Schaefer, M.V.; Grassian, V.H.; Scherer, M.M. Interpreting nanoscale size-effects in aggregated Fe-oxide suspensions: Reaction of Fe(II) with Goethite. *Geochimica Et Cosmochimica Acta* **2008**, *72*(5), 1365-1380.
10. Tiraferri, A.; Sethi, R. Enhanced transport of zerovalent iron nanoparticles in saturated porous media by guar gum. *J Nanopart Res* **2009**, *11*(3), 635-645.
11. Saleh, N.; Kim, H.J.; Phenrat, T.; Matyjaszewski, K.; Tilton, R.D.; Lowry, G.V. Ionic strength and composition affect the mobility of surface-modified Fe-0 nanoparticles in water-saturated sand columns. *Environmental Science & Technology* **2008**, *42*(9), 3349-3355.
12. Dalla Vecchia, E.; Luna, M.; Sethi, R. Transport in Porous Media of Highly Concentrated Iron Micro- and Nanoparticles in the Presence of Xanthan Gum. *Environmental Science & Technology* **2009**, *43*(23), 8942-8947.
13. Phenrat, T.; Saleh, N.; Sirk, K.; Tilton, R.D.; Lowry, G.V. Aggregation and sedimentation of aqueous nanoscale zerovalent iron dispersions. *Environmental Science & Technology* **2007**, *41*(1), 284-290.
14. Bradford, S.A.; Yates, S.R.; Bettahar, M.; Simunek, J. Physical factors affecting the transport and fate of colloids in saturated porous media. *Water Resources Research* **2002**, *38*(12), Doi 10.1029/2002wr001340.
15. Saleh, N.; Sirk, K.; Liu, Y.Q.; Phenrat, T.; Dufour, B.; Matyjaszewski, K.; Tilton, R.D.; Lowry, G.V. Surface modifications enhance nanoiron transport and NAPL targeting in saturated porous media. *Environmental Engineering Science* **2007**, *24*(1), 45-57.
16. He, F.; Zhao, D.Y. Preparation and characterization of a new class of starch-stabilized bimetallic nanoparticles for degradation of chlorinated hydrocarbons in water. *Environmental Science & Technology* **2005**, *39*(9), 3314-3320.
17. Phenrat, T.; Saleh, N.; Sirk, K.; Kim, H.J.; Tilton, R.D.; Lowry, G.V. Stabilization of aqueous nanoscale zerovalent iron dispersions by anionic polyelectrolytes: adsorbed anionic polyelectrolyte layer properties and their effect on aggregation and sedimentation. *J Nanopart Res* **2008**, *10*(5), 795-814.

18. Tiraferri, A.; Chen, K.L.; Sethi, R.; Elimelech, M. Reduced aggregation and sedimentation of zero-valent iron nanoparticles in the presence of guar gum. *Journal of Colloid and Interface Science* **2008**, *324*(1-2), 71-79.
19. Comba, S.; Sethi, R. Stabilization of highly concentrated suspensions of iron nanoparticles using shear-thinning gels of xanthan gum. *Water Research* **2009**, *43*(15), 3717-3726.
20. Gonzalez, J.M.; Muller, A.J.; Torres, M.F.; Saez, A.E. The role of shear and elongation in the flow of solutions of semi-flexible polymers through porous media. *Rheol Acta* **2005**, *44*(4), 396-405.
21. Deshpande, P.A.; Shonnard, D.R. Modeling the effects of systematic variation in ionic strength on the attachment kinetics of Pseudomonas fluorescens UPER-1 in saturated sand columns. *Water Resources Research* **1999**, *35*(5), 1619-1627.
22. Song, L.; Elimelech, M. Dynamics of Colloid Deposition in Porous-Media - Modeling the Role of Retained Particles. *Colloids and Surfaces a-Physicochemical and Engineering Aspects* **1993**, *73*, 49-63.
23. Gargiulo, G.; Bradford, S.A.; Simunek, J.; Ustohal, P.; Vereecken, H.; Klumpp, E. Transport and deposition of metabolically active and stationary phase Deinococcus radiodurans in unsaturated porous media. *Environmental Science & Technology* **2007**, *41*(4), 1265-1271.
24. Johnson, W.P.; Pazmino, E.; H., M. Direct observations of colloid retention in granular media in the presence of energy barriers, and implications for inferred mechanisms from indirect observations. *Water Research* **2010**, *44*(4), 1158-1169.
25. Johnson, W.P.; Li, X.Q.; Yal, G. Colloid retention in porous media: Mechanistic confirmation of wedging and retention in zones of flow stagnation. *Environmental Science & Technology* **2007**, *41*(4), 1279-1287.
26. Camesano, T.A.; Unice, K.M.; Logan, B.E. Blocking and ripening of colloids in porous media and their implications for bacterial transport. *Colloids and Surfaces a-Physicochemical and Engineering Aspects* **1999**, *160*(3), 291-308.
27. Tosco, T.; Tiraferri, A.; Sethi, R. Ionic Strength Dependent Transport of Microparticles in Saturated Porous Media: Modeling Mobilization and Immobilization Phenomena under Transient Chemical Conditions. *Environmental Science & Technology* **2009**, *43*(12), 4425-4431.
28. Mays, D.C.; Hunt, J.R. Hydrodynamic aspects of particle clogging in porous media. *Environmental Science & Technology* **2005**, *39*(2), 577-584.
29. Emmanuel, S.; Berkowitz, B. Mixing-induced precipitation and porosity evolution in porous media. *Advances in Water Resources* **2005**, *28*(4), 337-344.
30. Kildsgaard, J.; Engesgaard, P. Numerical analysis of biological clogging in two-dimensional sand box experiments. *Journal of Contaminant Hydrology* **2001**, *50*(3-4), 261-285.
31. Thullner, M.; Schroth, M.H.; Zeyer, J.; Kinzelbach, W. Modeling of a microbial growth experiment with bioclogging in a two-dimensional saturated porous media flow field. *Journal of Contaminant Hydrology* **2004**, *70*(1-2), 37-62.
32. Pearson, J.R.A.; Tardy, P.M.J. Models for flow of non-Newtonian and complex fluids through porous media. *J Non-Newton Fluid* **2002**, *102*(2), 447-473.
33. Cross, M.M. Rheology of non-Newtonian fluids: A new flow equation for pseudoplastic systems. *Journal of Colloid Science* **1965**, *20*(5), 417-437.
34. Kozeny, J. Uber Kapillare Leitung des Wasser im Boden. *Sitzungsberichte der Akademie der Wissenschaften Wien* **1927**, ***136***, 106-271.
35. Comba, S.; Dalmazzo, D.; Santagata, E.; Sethi, R. Rheological characterization of xanthan suspensions of nanoscale iron for injection in porous media. *Journal of Hazardous Materials*, *In Press, Accepted Manuscript*.
36. Wyatt, N.B.; Liberatore, M.W. Rheology and Viscosity Scaling of the Polyelectrolyte Xanthan Gum. *J Appl Polym Sci* **2009**, *114*(6), 4076-4084.

37. Lopez, X.; Valvatne, P.H.; Blunt, M.J. Predictive network modeling of single-phase non-Newtonian flow in porous media. *Journal of Colloid and Interface Science* **2003**, *264*(1), 256-265.
38. Bird, R.B. *Transport phenomena*; Wiley: New York,, 1960.
39. Perrin, C.L.; Tardy, P.M.J.; Sorbie, K.S.; Crawshaw, J.C. Experimental and modeling study of Newtonian and non-Newtonian fluid flow in pore network micromodels. *Journal of Colloid and Interface Science* **2006**, *295*(2), 542-550.
40. Bradford, S.A.; Simunek, J.; Bettahar, M.; Van Genuchten, M.T.; Yates, S.R. Modeling colloid attachment, straining, and exclusion in saturated porous media. *Environmental Science & Technology* **2003**, *37*(10), 2242-2250.
41. Atekwana, E.A.; Richardson, D.S. Geochemical and isotopic evidence of a groundwater source in the Corral Canyon meadow complex, central Nevada, USA. *Hydrological Processes* **2004**, *18*(15), 2801-2815.
42. Tosco, T.; Sethi, R. MNM1D: a numerical code for colloid transport in porous media: implementation and validation. *American Journal of Environmental Sciences* **2009**, *5*(4), 517-525.
43. Coleman, T.F.; Li, Y.Y. An interior trust region approach for nonlinear minimization subject to bounds. *Siam J Optimiz* **1996**, *6*(2), 418-445.

ACKNOWLEDGMENT: The work was co-funded by the European Union project AQUAREHAB (FP7 - Grant Agreement Nr. 226565). The transport simulations were run on the Ditag workstation Xeon X5660.

SUPPORTING INFORMATION AVAILABLE.

Summary of model parameters (p. S1), detailed description of the modeled phases (p. S4) and modified Cross model (p. S5), properties of sand and iron materials (p. S7), and detailed mass balances (p. S8) are provided in the Supporting Information. Profiles of deposited particles (p. S9) and of the factors contributing to permeability reduction (p. S10) are also reported. This information is available free of charge via the Internet at http://pubs.acs.org/

CAPTIONS:

Table 1: Fitted coefficients for micro- and nanoiron column tests.

Figure 1: Isotherms of colloid deposition and release for the general kinetic formulation of eq. (9). Curves are obtained using typical values of iron transport tests for $k_{a,i}$, $k_{d,i}$, ρ_b, ε_m. $\beta_i = 1$ in all cases. $A_i > 0$ for ripening, $A_i = 0$ for linear isotherm, $A_i < 0$ for blocking.

Figure 2: Model fitted and experimental breakthrough curves (a-c and g-i) and pressure drop (d-f and j-l) at column ends as a function of time, for microiron (M26X, M7X, M7XIS) and nanoiron (N26X, N7X, N7XIS). Experimental breakthrough curves of colloid concentration were sampled with a time interval of 1 s, plotted interval was adopted purely for graphical reasons.

Figure 3: Total iron concentration profiles c_{tot}/c_0 (a) and normalized permeability coefficient K/K_0 (b) along the column at the end of the injection phase. Simulated and measured profiles are reported as total (suspended plus retained) iron concentration, referred to the initial porosity according to $c_{tot} = c + (\rho_b s)/n$.

Tables and Figures:

Table 1:

Parameter		Test					
		M26X	M7X	M7XIS	N26X	N7X	N7XIS
ρ_s	(kg/m^3)	$1.26 \bullet 10^{3}$	$1.26 \bullet 10^{3}$	$2.48 \bullet 10^{3}$	$3.35 \bullet 10^{3}$	$3.05 \bullet 10^{3}$	$1.13 \bullet 10^{3}$
θ	(-)	$3.47 \bullet 10^{-2}$	$1.68 \bullet 10^{-2}$	$8.28 \bullet 10^{-3}$	$1.04 \bullet 10^{-3}$	$1.52 \bullet 10^{-3}$	$5.63 \bullet 10^{-4}$
α_γ	(g/m^3)	0.82	0.85	0.94	0.88	0.88	0.79
$k_{ax,1}$	(1/s)	$3.53 \bullet 10^{-3}$	$7.25 \bullet 10^{-3}$	$1.08 \bullet 10^{-4}$	$2.47\ 10^{-5}$	$5.21 \bullet 10^{-5}$	$1.00 \bullet 10^{-5}$
$k_{dx,1}$	(1/s)	$2.98 \bullet 10^{-3}$	$6.68 \bullet 10^{-3}$	$2.13 \bullet 10^{-3}$	$6.11 \bullet 10^{-4}$	$1.72 \bullet 10^{-3}$	$1.38 \bullet 10^{-3}$
$k_{aw,1}$	(1/s)	$8.17 \bullet 10^{-2}$	$1.68 \bullet 10^{-1}$	$6.82 \bullet 10^{-1}$	$4.82 \bullet 10^{-5}$	$2.43 \bullet 10^{-4}$	$2.22 \bullet 10^{-5}$
$k_{dw,1}$	(1/s)	$2.05 \bullet 10^{-2}$	$4.91 \bullet 10^{-2}$	$8.56 \bullet 10^{-4}$	$5.06 \bullet 10^{-3}$	$1.33 \bullet 10^{-2}$	$4.12 \bullet 10^{-2}$
β_1	(-)	0.25	0.28	1.09	0.55	0.58	0.79
A_1	(-)	-3.63	-4.40	-864.9	851.22	936.34	17652
$k_{ax,2}$	(1/s)	$2.08 \bullet 10^{-4}$	$2.95 \bullet 10^{-4}$	$1.47 \bullet 10^{-3}$	$1.79 \bullet 10^{-3}$	$2.01 \bullet 10^{-3}$	$8.46 \bullet 10^{-3}$
$k_{dx,2}$	(1/s)	$1.97 \bullet 10^{-4}$	$9.54 \bullet 10^{-5}$	$4.05 \bullet 10^{-5}$	$1.89 \bullet 10^{-3}$	$4.40 \bullet 10^{-3}$	$1.35 \bullet 10^{-3}$
$k_{aw,2}$	(1/s)	$2.09 \bullet 10^{-3}$	$3.23 \bullet 10^{-3}$	$6.40 \bullet 10^{-4}$	$3.48 \bullet 10^{-2}$	$1.57 \bullet 10^{-2}$	$4.27 \bullet 10^{-1}$
$k_{dw,2}$	(1/s)	$2.00 \bullet 10^{-3}$	$8.00 \bullet 10^{-4}$	$3.07 \bullet 10^{-3}$	$1.72 \bullet 10^{-4}$	$1.10 \bullet 10^{-3}$	$1.64 \bullet 10^{-2}$
β_2	(-)	0.009	0.01	0.25	0.081	0.074	0.34

Figure 1:

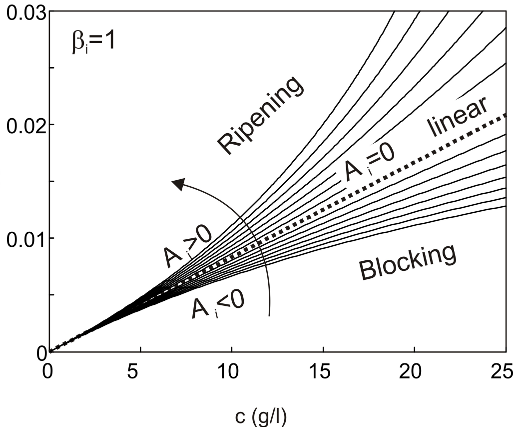
β_i=1
Ripening
A_i>0
A_i=0
linear
A_i<0
Blocking
s (-)
0.03
0.02
0.01
0
c (g/l)
0
5
10
15
20
25

Figure 2:

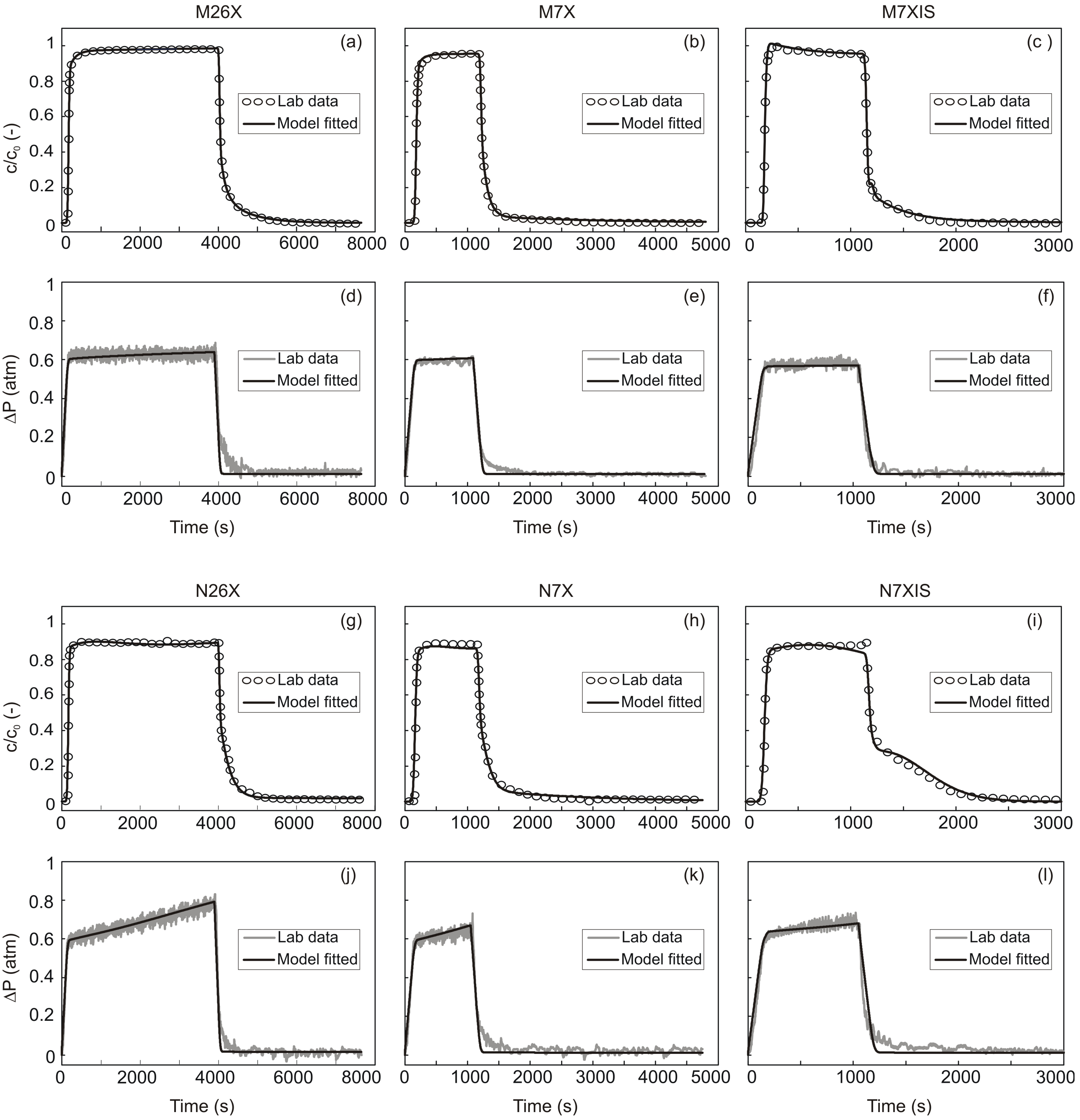
M26X
M7X
M7XIS
(a)
(b)
(c)
(d)
(e)
(f)
N26X
N7X
N7XIS
(g)
(h)
(i)
(j)
(k)
(l)
c/c_0 (-)
ΔP (atm)
Time (s)
Lab data
Model fitted
0
0.2
0.4
0.6
0.8
1
0
2000
4000
6000
8000
1000
3000
5000

Figure 3:

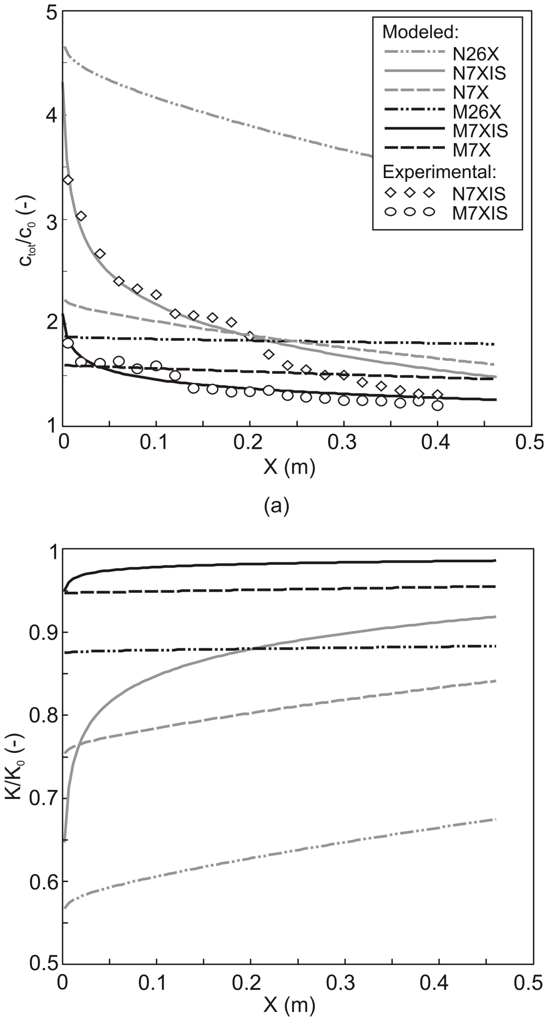
Modeled:
N26X
N7XIS
N7X
M26X
M7XIS
M7X
Experimental:
N7XIS
M7XIS
c_{tot}/c_0 (-)
X (m)
5
4
3
2
1
0
0.1
0.2
0.3
0.4
0.5
K/K_0 (-)
1
0.9
0.8
0.7
0.6
0.5

(a)

(b)

BRIEF: A flow-transport model is proposed and applied to experimental data for the simulation of transport in porous media of highly concentrated non-Newtonian suspensions of iron colloids for groundwater remediation.